Supplementary Methods

P2R Precision Apparatus for Real Time Synchrotron Tomographic Imaging with Load, Displacement and Rotation Control

X-ray computed microtomography is used to investigate internal structure in many disciplines. When applied to biomechanics, a loading device is required that can grip/cup the joint, maintain hydration, apply displacements, and measure load while performing highly accurate rotation to allow radiographic projections to be acquired through 180 or 360 degrees (for parallel or cone beam, respectively). To achieve this, a bespoke precision apparatus was designed and commissioned. The apparatus has been used in a wide range of applications including semi-solid deformation [1], frozen soil behaviour [2], granular flows [3], crack propagation [4], high temperature self-healing ceramics [5], and deformation of electrospun biodegradable fibres [6].

The apparatus was developed to achieve a series of rigorous requirements: (i) tightly controlled axial load and rotation motion with axial alignment suitable for synchrotron x-ray microtomography imaging with sub-micron resolution (ii) no obscuration of the beam path during data acquisition, either from the apparatus or the environmental hydration cell (iii) overall system stability sufficient to maintain sub-micron accuracy in rotation, axial displacement, axial alignment and applied load over the measurement period, which may range from seconds to hours depending on the physical characteristics of the material under investigation.

The load range was specified as ±1-500 N with extension of 0-150 mm and specimen rotation over ±0-360°, including continuous rotation. The specified encoded accuracy for load is 0.1 N, for extension is 50 nm and for rotation is 0.001°.

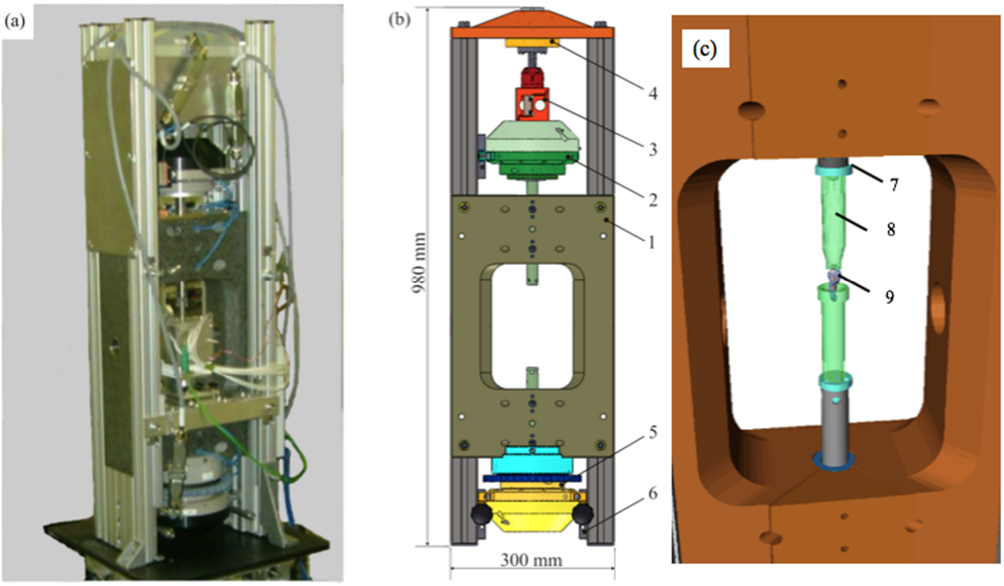

Suppl. Fig. S1. (a) *photograph of P2R biomechanical tomography apparatus.* ***(b)*** *Schematic showing: 1. granite frame with shaft air brushings; 2. upper motor and thrust air bearing; 3. load cell and linear strain encoder; 4. screw shaft motor; 5. lower motor and thrust air bearing; 6. further manual displacement adjustment.* ***(c)*** *Zoom of specimen area showing: 7. 20 mm rotation shafts; 8. 3D printed specimen grips; and 9. murine knee joint.*

To enable a broad range of applications, not just biomechanics, the system was constructed around a granite base frame to enable temperature from -100 to 1600 ºC to be achieved in the specimen area while retaining dimensional stability. The specimen environmental cell region is a 230 mm high, 150 mm wide rectangular aperture cut in the granite frame. The granite frame houses two 20 mm diameter inline rotating shafts that are mounted in radial air bushings with an alignment of >50 nm, (Suppl. Fig. S1). A 150 mm thrust disc is located at the end of each shaft that provides the register for three 50 mm circular pad air-bearings on one side and a single 100 mm circular pad air bearing on the other. This air-bearing arrangement supports rotation, axial loading and associated displacement with minimum friction. The two specimen rotation shafts are mounted and housed in similar assemblies. In this respect the air-bearing support, servomotor drive and shaft rotary encoding use identical components. The servomotors are of the frameless type and as a consequence the servomotor rotors are attached directly to the shafts. This avoids the possibility of vibration introduced by the misalignment commonly associated with mechanical shaft coupling.

Optical angle encoding combined with 20 μm graduation accuracy and servomotor control ensures synchronous rotation is achieved with a better than 0.001° differential error. For high-speed synchrotron work, the system has been tested at continuous rotation speeds of up to 2 Hz, and faster speeds may be achievable. It can also operate at low continuous speeds as well as stepped motion at angular increments of less than 0.1°. The top/bottom can be rotated independently to provide set values of offset torsion or continuous variation torsion if required. The axial movement of the load-cell and attached upper rotary shaft assembly is provided by the motion of a 16 mm diameter, 5 mm pitch, 3 start, precision ball screw assembly. The screw shaft is rotationally stationary and is attached to the bottom of the load-cell through the fixed cylindrical flexure. The screw shaft nut is held captive in an angular contact bearing and is rotationally driven by a brushless, frameless torque motor. The motor, ball screw and thrust bearing are mounted on a bracket that is rigidly attached to the two support rails bolted to the granite base frame.

This apparatus was used for both the physiologically-representative whole joint loading model, and the high accuracy localised indenter loading model detailed in this manuscript.

Physiologically-representative whole joint loading model

Unfortunately, the full range of mechanical stimuli involved in joint health and disease is poorly characterised and would require long duration and varied application, making it unfeasible to replicate during a synchrotron experiment. Therefore, we chose to use the non-invasive murine hind-limb loading model developed by De Souza et al. 2005 [7] and characterised in adapted form for use in the technique developed by Poulet et al. 2011 [8]. The loading model enables highly reproducible loads to be applied to the murine knee joint, producing reproducible strains. Use of this model has been shown to enable adjustable, non-invasive loading to murine joints that replicates physiological loading conditions; increasing the number of loading bouts and their magnitude over a two week-long period generates articular cartilage lesions that advance to spontaneous osteoarthritis [8].

Here, the technique developed by Poulet et al. [8] was further improved upon by first scanning the knees, and then custom 3D printing the cups (Fig. 1A main paper) to hold and apply load to the joint during synchrotron imaging, enabling even more accurate and repeatable application of load, as detailed in Methods and below.

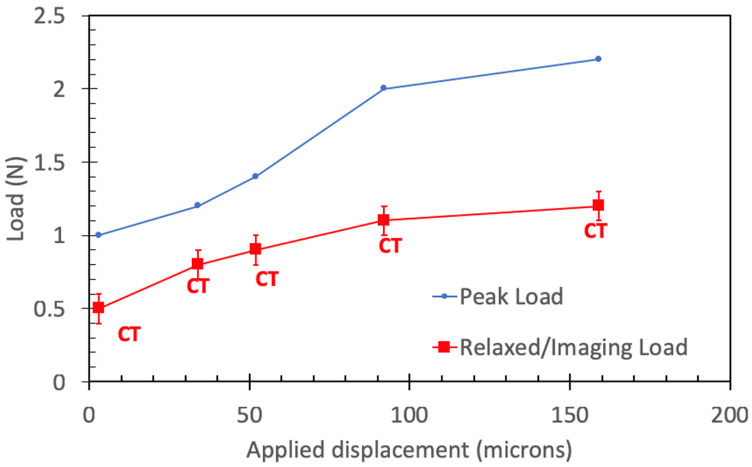

Suppl. Fig. S2. *Loading sequence for the physiologically-representative whole joint model applied to the 60 week STR/Ort mouse knee joint showing: preloading to a peak load of 1.0±0.1 N, 10 minutes relaxation, sCT scan acquisition under a stable load of 0.5±0.1 N; intermediate scans conducted after compression steps associated with peak load increases of 0.2N; final scans after compression to peak loads exceeded 2N.*

Loading was quasi-static, with controlled vertical motion of 5 microns/sec until target loads were reached, followed by a relaxation/stabilization wait time of 10 minutes before imaging. As shown in Fig. S2, an initial target peak load of 1.0 N was applied, with 10 minutes of relaxation followed by CT scanning, where loads had stabilized to 0.5 N. This initial scan volume was used as the reference for digital volume correlation. Sample compression was then applied to generate load increases of 0.2N, with subsequent relaxation and scanning. Final scans were collected as compression generated loads exceeding 2.0N. The sequence of small load increases followed by larger load increases aids in sample stabilization and allows visualization and analysis of the deformation sequence. Peak loads decreased by approximately 50% during sample relaxation, and loads during scanning were steady within the resolution limits of the measurement system, ±0.1 N.

Indenter loading model

The loading model of Poulet et al. [7] enables whole joint imaging, however, the loads applied to the tibial plateau depend on the shape of the femur. To enable high accuracy probing of localized mechanical properties that is repeatable and only dependent upon the mechanical structure of the tibial plateau, we developed a new additional loading model that replicates some aspects of the different types of physiological loading, but with even higher repeatability. This was done using a round diamond Vickers indenter (250μm radius). The tibia was positioned with the long axis oriented vertically, medial plateau centred over the mid-shaft. The indenter was mounted on a small x-y translation stage within the loading rig, allowing micron-scale motions in the horizontal plane perpendicular to the tibia axis. The indenter tip was visualized using synchrotron x-ray imaging and positioned in the centre of the medial plateau, as viewed in both the Medial-Lateral and Anterior-Posterior planes. The loading direction was vertical, aligned with the tibia long axis. The loading sequence was identical to that used for the whole joint (Fig. S2).

Displacement and Strain Maps

The fundamental digital volume correlation (DVC) process generates displacement vectors associated with a point cloud. Point clouds are sets of discrete locations generated within the voxel coordinate system of the reference tomography volume, and therefore all associated displacement and strain data maintain a consistent spatial relationship with the scans. Co-visualization of microstructure and displacement/strain were generated by importing both the image data and the associated measurement results into Avizo, with image data rendering applied to the scan data and coloured fringe plots generated through standard data plotting methods. Adding semi-transparency to the data fringe plots allows the visualization of sample microstructure in concert with measurement data.

Estimation of image quality using signal-to-noise-ratio (SNR)

The signal-to-noise ratio describes the distance of bone intensity distribution from the background (air) intensity distribution and is defined as:

$$SNR = \frac{\mu_{bone} - \mu_{air}}{\sqrt{\sigma_{bone}^{2} + \sigma_{air}^{2}}}$$

where μ_{bone} and μ_{air} are the mean intensities of patches of 32 x 32 bone and background pixels, respectively, and where σ_{bone} and σ_{air} are the standard deviation of pixel intensity in the same object bone and background patch. Eight pairs of patches were chosen randomly across the field of view. The areas used for the measurement of bone grey levels were selected inside the matrix (osteons) and excluded the osteocyte lacunae [9]. The air areas were selected outside the sample.

Determination of flux

The conditions for each beam type used are given in Table ST1, and typical dose rates at different bio-imaging beamlines are reported in Table ST2. Note, all images in the main paper were taken with Setup 1. The effects of the different imaging setups described in Table ST1 on image quality and digital volume correlation performance are further illustrated in Figure S3.

Suppl. Table ST1: *Parameters of the imaging setup together with the corresponding estimated: radiation dose, signal-to-noise ratio and DVC accuracy (subvolume size: 48 voxels).*

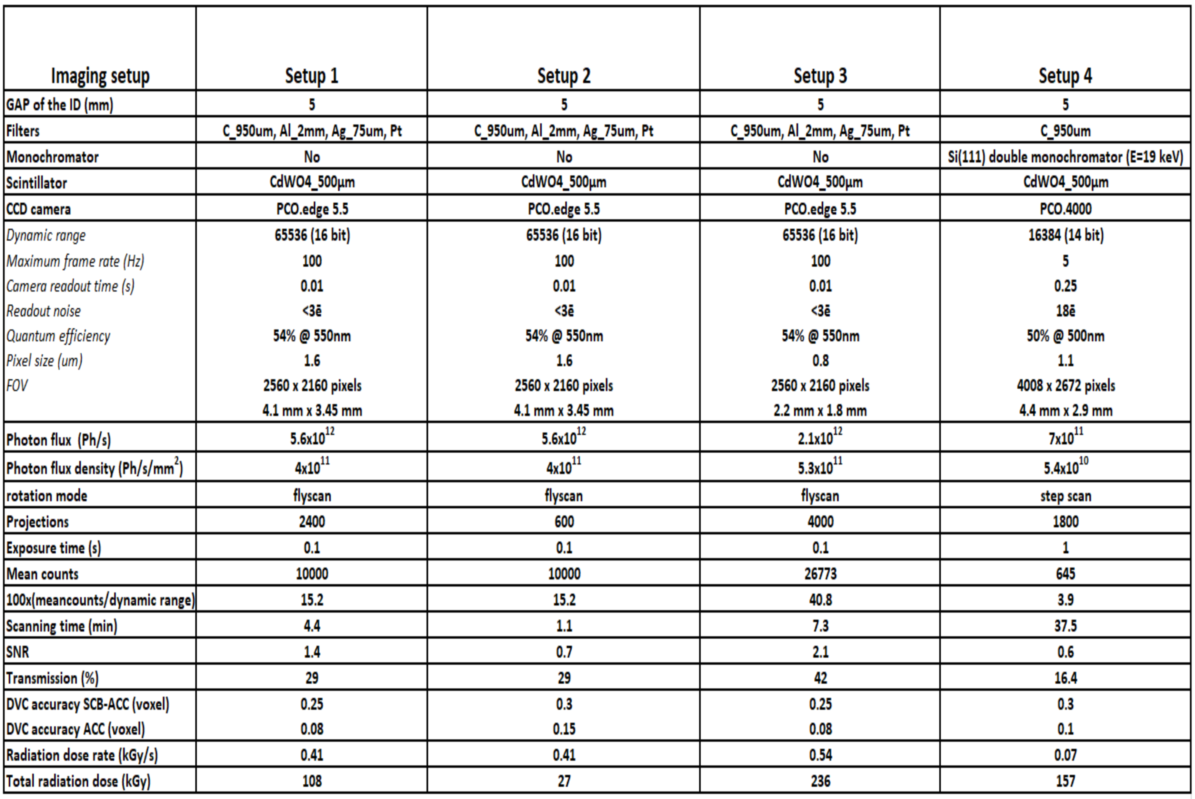

Imaging setup	Setup 1	Setup 2	Setup 3	Setup 4
GAP of the ID (mm)	5	5	5	5
Filters	C_950um, Al_2mm, Ag_75um, Pt	C_950um, Al_2mm, Ag_75um, Pt	C_950um, Al_2mm, Ag_75um, Pt	C_950um
Monochromator	No	No	No	Si(111) double monochromator (E=19 keV)
Scintillator	CdWO4_500µm	CdWO4_500µm	CdWO4_500µm	CdWO4_500µm
CCD camera	PCO.edge 5.5	PCO.edge 5.5	PCO.edge 5.5	PCO.4000
Dynamic range	65536 (16 bit)	65536 (16 bit)	65536 (16 bit)	16384 (14 bit)
Maximum frame rate (Hz)	100	100	100	5
Camera readout time (s)	0.01	0.01	0.01	0.25
Readout noise	<3ē	<3ē	<3ē	18ē
Quantum efficiency	54% @ 550nm	54% @ 550nm	54% @ 550nm	50% @ 500nm
Pixel size (um)	1.6	1.6	0.8	1.1
FOV	2560 x 2160 pixels 4.1 mm x 3.45 mm	2560 x 2160 pixels 4.1 mm x 3.45 mm	2560 x 2160 pixels 2.2 mm x 1.8 mm	4008 x 2672 pixels 4.4 mm x 2.9 mm
Photon flux (Ph/s)	$5.6x10^{12}$	$5.6x10^{12}$	$2.1x10^{12}$	$7x10^{11}$
Photon flux density (Ph/s/mm^2)	$4x10^{11}$	$4x10^{11}$	$5.3x10^{11}$	$5.4x10^{10}$
rotation mode	flyscan	flyscan	flyscan	step scan
Projections	2400	600	4000	1800
Exposure time (s)	0.1	0.1	0.1	1
Mean counts	10000	10000	26773	645
100x(meancounts/dynamic range)	15.2	15.2	40.8	3.9
Scanning time (min)	4.4	1.1	7.3	37.5
SNR	1.4	0.7	2.1	0.6
Transmission (%)	29	29	42	16.4
DVC accuracy SCB-ACC (voxel)	0.25	0.3	0.25	0.3
DVC accuracy ACC (voxel)	0.08	0.15	0.08	0.1
Radiation dose rate (kGy/s)	0.41	0.41	0.54	0.07
Total radiation dose (kGy)	108	27	236	157

Suppl. Table ST2. *Dose rates from in situ synchrotron tomography experiments*

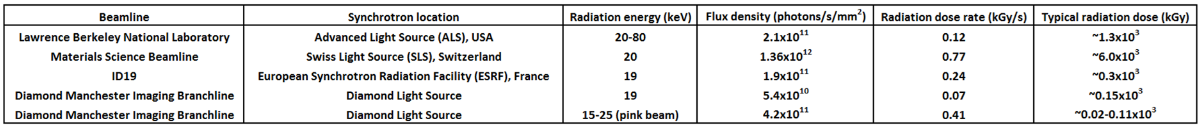

Beamline	Synchrotron location	Radiation energy (keV)	Flux density (photons/s/mm^2)	Radiation dose rate (kGy/s)	Typical radiation dose (kGy)
Lawrence Berkeley National Laboratory	Advanced Light Source (ALS), USA	20-80	$2.1x10^{11}$	0.12	$\sim1.3x10^{3}$
Materials Science Beamline	Swiss Light Source (SLS), Switzerland	20	$1.36x10^{12}$	0.77	$\sim6.0x10^{3}$
ID19	European Synchrotron Radiation Facility (ESRF), France	19	$1.9x10^{11}$	0.24	$\sim0.3x10^{3}$
Diamond Manchester Imaging Branchline	Diamond Light Source	19	$5.4x10^{10}$	0.07	$\sim0.15x10^{3}$
Diamond Manchester Imaging Branchline	Diamond Light Source	15-25 (pink beam)	$4.2x10^{11}$	0.41	$\sim0.02\text{-}0.11x10^{3}$

Monochromatic Beam

The monochromatic X-ray beam at 19 keV was selected by combining the mini-beta undulator with a Si(111) double-crystal monochromator ($\frac{\Delta E}{E} = 10^{-4}$). The flux was characterised using an ionization chamber and measured to be 700 Gph/s (Table ST1, setup 4).

Pink beam

To estimate the flux in pink beam, we used the undulator code Xus available in XOP 2.4 to calculate the spectrum for an ideal elliptical or planar undulator using the Bessel function approximation [10]. The flux was calculated with the undulator placed in a low beta section (Diamond mini-beta U22) at different ID gaps. The flux attenuation introduced by the filters (1.3mm pyrolytic graphite, 3.2 mm aluminium, 75 µm silver) and the mirror (Pt stripe) was also assessed using the Xpower code available in XOP. The purpose of the filters is to reduce the heat-load by absorbing low-energy radiation, whereas the mirror is to direct and focus the beam [11]. The undulator radiation depends on the electron energy in the storage ring, the undulator spatial period, and the deflection parameter, K:

$$K = 0.934 \times \lambda_u \times B_0$$

where λ_u [cm] is the undulator spatial period and B_0 [T] is the effective magnetic field.

The parameters used for the simulations are reported in Suppl. Table ST3. The effective magnetic field and the deflection parameter vary with the gap between the magnet arrays (Suppl. Fig. S4a). The spectrum of the undulator U22 is characterised by multiple narrowband peaks (Suppl. Fig. S4b, 12 harmonics between 5-30 keV). The filtered spectrum used in our in situ experiments has only 6 harmonics between 16-25 keV (Suppl. Fig. S4a).

Our simulations were compared with flux experiments obtained on the Diamond-Manchester Imaging Branchline. The measurements were made using an ID gap of 5 mm by combining the undulator with a water-cooled double crystal Si 111 monochromator (DCM). The energy range was 5-30 keV with a resolution of about 10 eV. A good agreement was found between the simulations and experiments (Suppl. Fig. S4b). It is worth mentioning that a precise simulation of the flux is difficult due to the variability of several factors such as spacing between the magnets, alignment errors of the magnets and small variations of beam current/energy.

Evaluation of radiation dose

The radiation dose represents the mean energy imparted to the tissue per unit mass by ionizing radiation. The radiation dose was measured in grays $[J/kg]$ and was estimated using a procedure used by Pacureanu et al. [9] and Barth et al. [12] in monochromatic beam. We adapted this method to pink beam by integrating the dose over the filtered spectrum. The radiation dose rate $D_r[Gy/s]$ is computed from the calculated flux $\psi(E)[ph/s/mm^2]$ and from the X-ray mass attenuation coefficient of cortical bone $\frac{\mu}{\rho}(E)[mm^2/g]$, available in the XOP database. The dose rate in pink and mono beam was calculated using these equations:

$$D_r(E)^{Pink} = \int_{E=5kV}^{30kV} \psi(E) \times E \times 1.6 \times 10^{-19} \times \frac{\mu}{\rho}(E)dE$$

Where

$$D_r(E)^{mono} = \psi(E) \times E \times 1.6 \times 10^{-19} \times \frac{\mu}{\rho}(E), \ (\phi(E) = \psi(E) \times E \times 1.6 \times 10^{-19}$$

is the energy density.

The total applied dose $D_t[Gy]$ is then obtained by multiplying the dose rate with the total exposure time $t[s]$: $D_t = D_r \times t$.

***Suppl. Table ST3**. Parameters used to simulate the undulator spectrum using the Xus program* in XOP 2.4

	E (GeV)	I (mA)	Mini-beta rms beam size Sigx (µm)	Mini-beta rms beam size Sigy (µm)	Mini-beta rms beam diverg. Sigx1 (µrad)	Mini-beta rms beam diverg. Sigy1 (µrad)	Period length (mm)	Num. of periods
Machine parameters	3.0147	300	-	-	-	-	-	-
Beam parameters (from U. Wagner [Rau et al., CXRD Workshop])	-	-	90	7	32	6	-	-
Undulator parameters	-	-	-	-	-	-	22	90

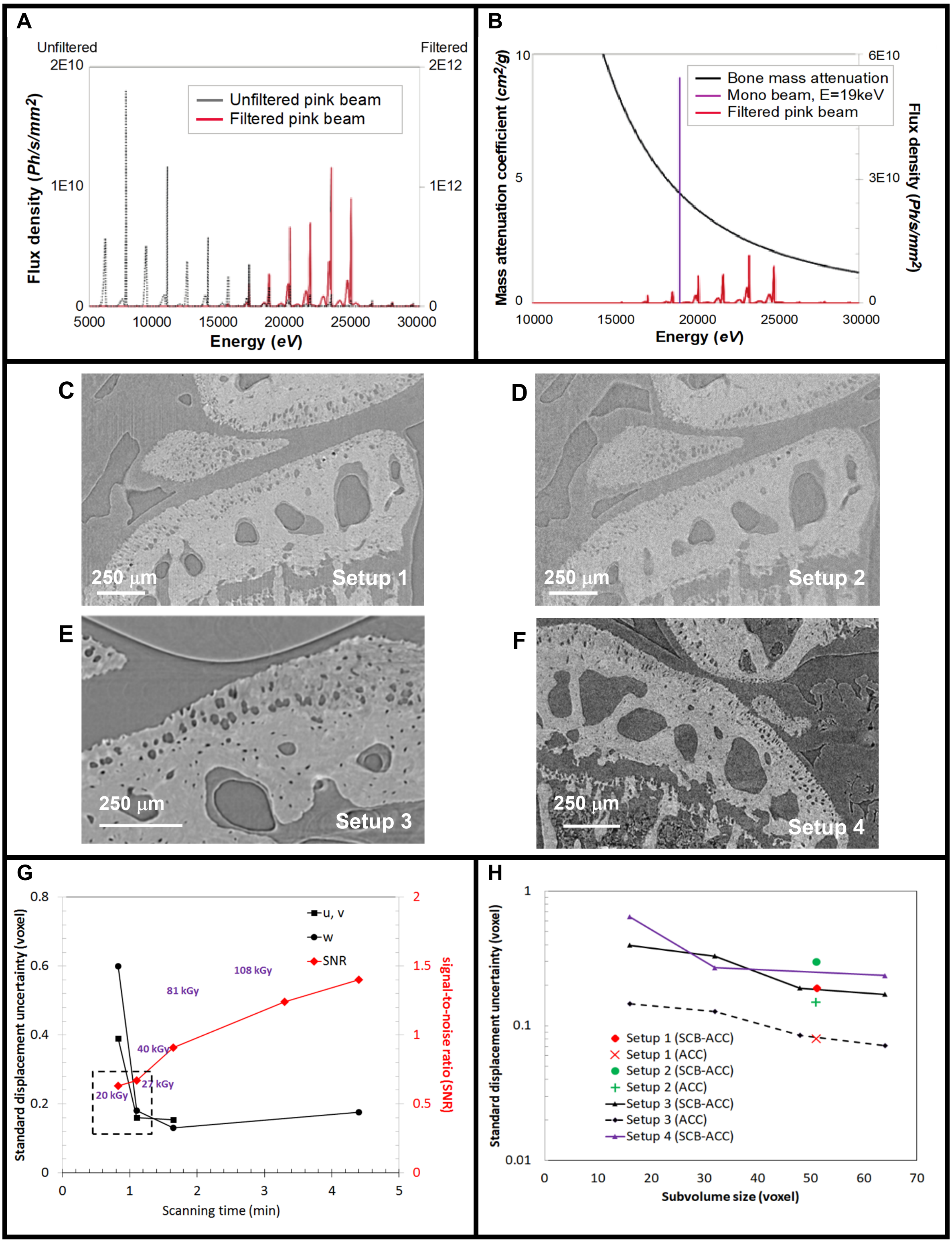

Suppl. Fig. S3. Optimising imaging conditions (refer to Suppl. Table ST1 for Setup details): ***(A)*** *Unfiltered and filtered pink beam flux.* ***(B)*** *Pink beam versus monochromatic beam flux in relation to the bone mass attenuation coefficient.* ***(C-F)*** *tomography sections for each Setup showing effect of signal-to-noise (SNR) ratio on image quality.* ***(G)*** *DVC accuracy (subvolume size 48 voxels), SNR and dose variation with number of projections (scan time) for Setup 1.* ***(H)*** *DVC accuracy versus subvolume size for each Setup.*

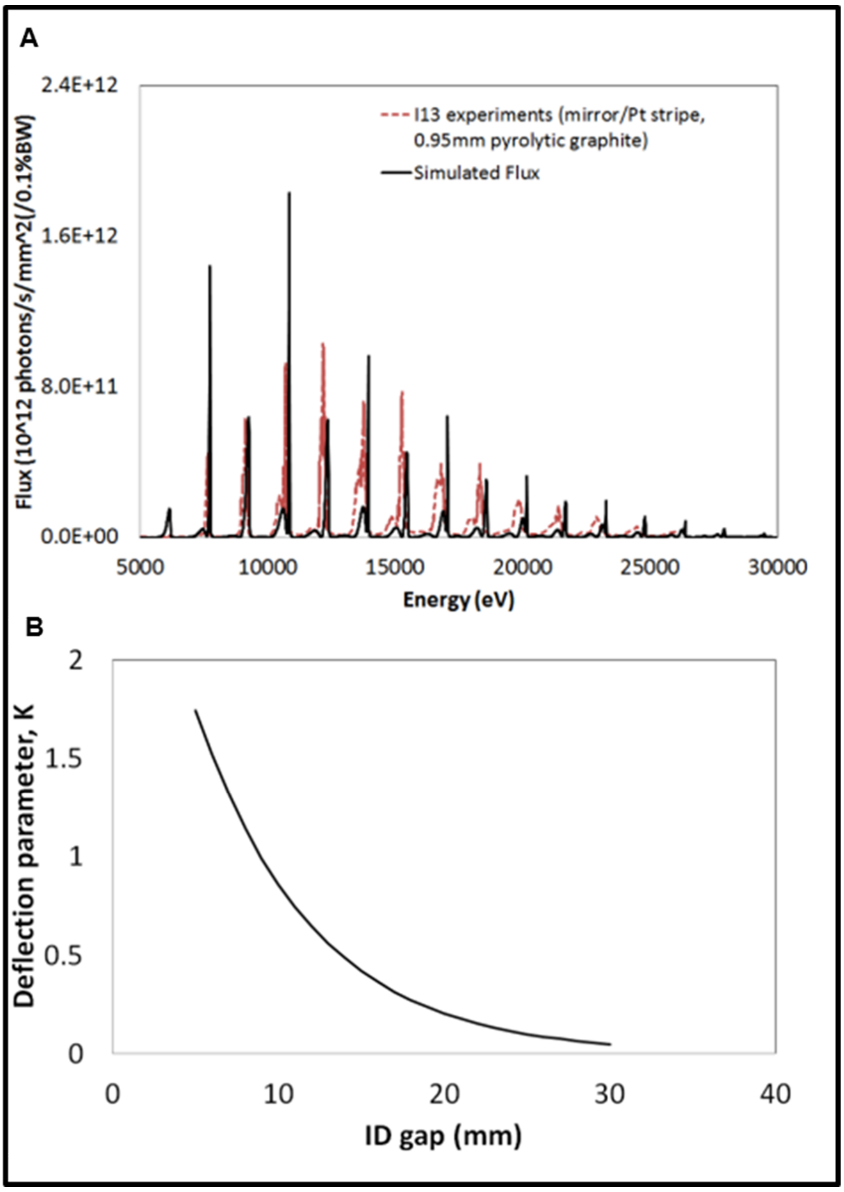

Suppl. Fig. S4. *Filtered spectrum at I13-2 as measured was compared to the calculated, showing that there are only 6 harmonics between 16-25 keV.*

Assessment of Experimental Repeatability

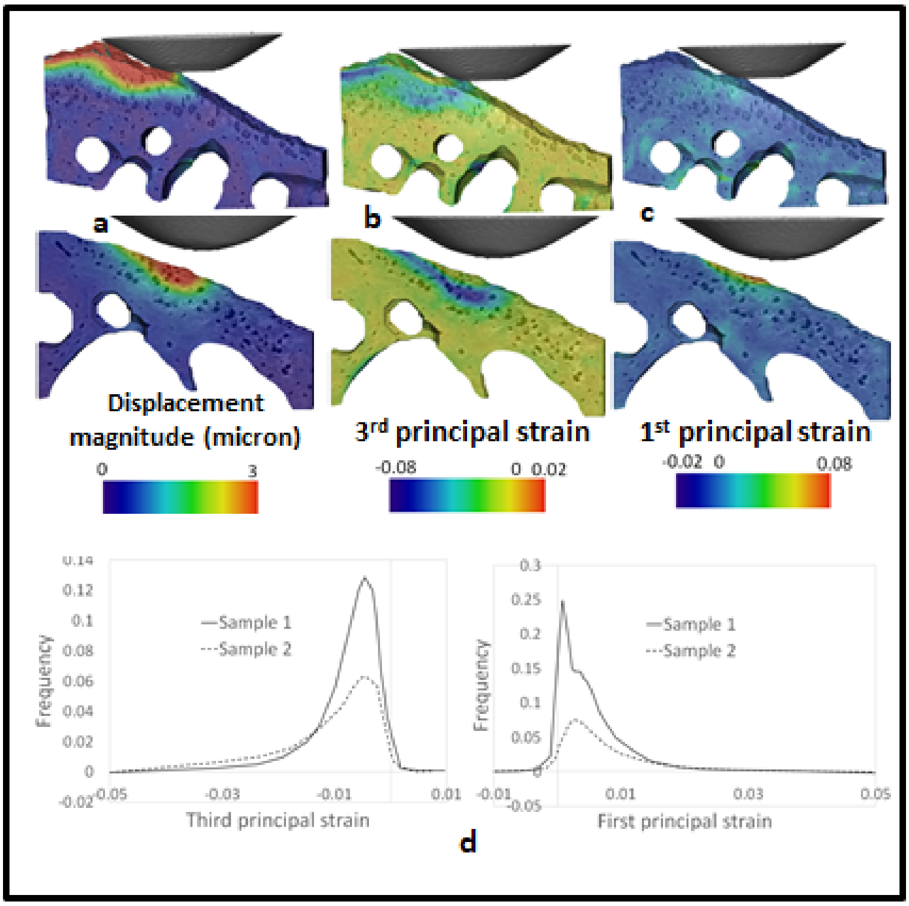

Suppl. Fig. S5. *Displacement magnitude and principal strain maps obtained by DVC after indentation of the medial compartment (2 specimens): High compression magnitude is observed in the calcified cartilage of the 20 week STR/Ort mice. Histograms of the first and third principal strains look similar and are both asymmetrical.*

References

1. Puncreobutr, C., Lee, P.D., Hamilton, R.W., and Phillion, A.B., "Quantitative 3D characterization of solidification structure and defect evolution in Al alloys", JOM: Volume 64, Issue 1 (2012), 89-95. /10.1007/s11837-011-0219-7
2. Ní Bhreasail, Á; Lee, P. D.; O'Sullivan, C; Fenton, C.H.; Hamilton, R.; Rockett, P.; Connolley, T, "In situ observation of cracks in frozen soil using synchrotron tomography", Permafrost and Periglacial Processes, Volume 23, Issue 2, pages 170–176, April 2012. /10.1002/ppp.1737
3. Kareh, K.M., Lee, P.D., Atwood, RC, Connolley, T., and Gourlay, C.M., "Revealing the micromechanisms behind semi-solid metal deformation with time-resolved X-ray tomography", Nature Commun., 5:5464, /10.1038/ncomms5464, July 2014.
4. Karagadde, S, Lee, PD, Cai, B, Fife, J.L., Azeem, M.A., Kareh, K.M., Puncreobutr, C., Tsivoulas, D., Connolley, T. & Atwood, R.C., "Transgranular liquation cracking of grains in the semi-solid state", Nature Commun., 5:9300, 10.1038/ncomms9300, 2015.
5. Sloof, WG., Pei, R., McDonald, SA., Fife, JL, Shen, L, Boatemaa, L, Farle, AS, Yan, K, Zhang, X, van der Zwaag, S, Lee, PD & Withers, PJ, "Repeated crack healing in MAX-phase ceramics revealed by 4D in situ synchrotron X-ray tomographic microscopy", Scientific Reports (2016) 23040, 10.1038/srep23040

6. Maksimcuka, J, Obata, A, Sampson, WW, Blanc, R, Gao, C, Withers, PJ, Tsigkou, O, Kasuga, T, Lee, PD, Poologasundarampillai, G, “X-ray tomographic imaging of tensile deformation modes of electrospun biodegradable polyester fibres, Frontiers in Materials, Dec. 21, 2017, https://doi.org/10.3389/fmats.2017.00043
7. De Souza, RL; Matsuura, M; Eckstein, F; Rawlinson, SCF; Lanyon, LE; Pitsillides, AA, “Non-invasive axial loading of mouse tibiae increases cortical bone formation and modifies trabecular organization: A new model to study cortical and cancellous compartments in a single loaded element”, Bone, 37 (6), 810-818, 2005, DOI: 10.1016/j.bone.2005.07.022
8. Poulet, B, Hamilton, RW, Shefelbine, S, Pitsillides, AA, “Characterizing a Novel and Adjustable Noninvasive Murine Joint Loading Model” Arthritis & Rheumatism, Vol. 63, No. 1, 2011, pp 137–147 DOI 10.1002/art.27765.
9. Pacureanu A, Langer M, Boller E, Tafforeau P, Peyrin F. Nanoscale imaging of the bone cell network with synchrotron X-ray tomography: optimization of acquisition setup. Med Phys. 2012;39:2229–38. doi:10.1118/1.3697525.
10. Dejus RJ, Sanchez del Rio M. XOP: A graphical user interface for spectral calculations and x-ray optics utilities. Rev Sci Instrum. 1996;67:3356–3356. doi:10.1063/1.1147376.
11. Fanis A De, Pešić ZD, Wagner U, Rau C. Fast X-ray imaging at beamline I13L at Diamond Light Source. J Phys Conf Ser. 2013;425:192014. doi:10.1088/1742-6596/425/19/192014.
12. Barth HD, Launey ME, MacDowell AA, Ager JW, Ritchie RO. On the effect of X-ray irradiation on the deformation and fracture behavior of human cortical bone. Bone. 2010;46:1475–85. doi:10.1016/j.bone.2010.02.025.